JGR Earth Surface

RESEARCH ARTICLE
10.1029/2022JF006781

Streamwise Turbulence Modulation in Non-Uniform Open-Channel Clay Suspension Flows

M. G. W. de Vet[1,2], R. Fernández[1,3], J. H. Baas[4], W. D. McCaffrey[5], and R. M. Dorrell[1]

[1]Energy and Environment Institute, University of Hull, Hull, UK, [2]Department of Geography and Environmental Studies, Saint Mary's University, Halifax, Nova Scotia, Canada, [3]Department of Civil and Environmental Engineering, Penn State University, University Park, PA, USA, [4]School of Ocean Sciences, Bangor University, Menai Bridge, UK, [5]School of Earth and Environment, University of Leeds, Leeds, UK

Key Points:

- Comparable to uniform flow, the combination of flow velocity and clay concentration influences the clay flow type in non-uniform flows
- Accelerating clay-laden flows adapt faster to velocity changes than decelerating flows; breaking clay bonds is easier than establishing them
- Adaptation timescales grow with clay concentration for decelerating clay-laden flows passing through a larger variety of clay flow types

Supporting Information:

Supporting Information may be found in the online version of this article.

Correspondence to:

M. G. W. de Vet,
m.de-vet@hull.ac.uk

Citation:

de Vet, M. G. W., Fernández, R., Baas, J. H., McCaffrey, W. D., & Dorrell, R. M. (2023). Streamwise turbulence modulation in non-uniform open-channel clay suspension flows. *Journal of Geophysical Research: Earth Surface*, *128*, e2022JF006781. https://doi.org/10.1029/2022JF006781

Received 16 JUN 2022
Accepted 19 JUL 2023

Abstract Cohesive sediment particles are ubiquitous in environmental flows. The cohesive properties of clay promote the formation of clay flocs and gels and relatively small suspended clay concentrations can enhance or suppress turbulence in a flow. Furthermore, flows are naturally non-uniform, varying in space and time, yet the dynamics of non-uniform open-channel clay suspension flows is poorly understood. For the first time, the adaptation time and length scales of non-uniform clay suspension flows were quantified using novel experiments with spatially varying but temporally uniform flow. Different levels of turbulence enhancement and attenuation were identified as the flow decelerates or accelerates. Results highlight that decelerating clay suspension flows crucially have a longer adaptation time than accelerating clay suspension flows. This is explained by the longer timescale required for the formation of bonds between cohesive particles in turbulence attenuated flows after deceleration than the rapid breakdown of bonds in turbulent flows after acceleration of clay suspension flows. This hysteresis is more pronounced for higher concentration decelerating flows that pass through a larger variety of clay flow types of turbulence enhancement and attenuation. These different adaptation time scales and associated clay flow type transitions are likely to affect clay flow dynamics in a variety of fluvial and submarine settings.

Plain Language Summary Flows in natural environments, such as rivers, estuaries, seas, and oceans, can transport sediment in suspension. The suspended sediment can increase or decrease turbulence in a flow, depending on the sediment concentration. Clay has the ability to form bonds between the individual particles and therefore even small concentrations are sufficient to alter turbulence levels in a flow. The amount of alteration of turbulence is known for uniform, constant flow conditions, but in natural environments, flows are often non-uniform. For example, flow variations can occur due to changes in river width or bed slope. The influence of these variations on clay suspension flows is unknown. New physical experiments were conducted where clay suspension flows were decelerated and accelerated. As the flow decelerates, turbulence in the flow is reduced and bonds between the suspended clay particles are established. Turbulence increases as the flow accelerates and clay bonds are broken. Decelerating flow requires more time to adjust to changes in velocity than accelerating flow, as establishing the bonds between clay particles requires more time than breaking them. This means that, especially for the decelerating flows, the influence of a change in velocity is noticeable further downstream.

1. Introduction

Cohesive sediment-laden flows are important in a wide range of natural environments, such as rivers, estuaries, shallow seas and deep oceans (Whitehouse et al., 2000; Winterwerp and van Kesteren, 2004), and in industrial settings (Ackers et al., 2001). For example, cohesive sediment supply to rivers can be increased by high-magnitude, low-frequency events, such as storms, floods and post-wildfire erosion (Sankey et al., 2017; Swanson, 1981), which occur more often because of climate change (Barbero et al., 2015; Geertsema et al., 2006; Reneau et al., 2007). Furthermore, cohesive sediment is common in submarine gravity currents, such as turbidity currents, hybrid events, mass flows and associated deposits (Talling et al., 2012). The increases in sediment transport can have major impacts on water quality and aquatic ecosystems, including fish habitats, and channel morphology (Smith et al., 2011). High suspended cohesive sediment concentrations modify flow dynamics by either enhancing (Baas & Best, 2002; Best et al., 1997) or dampening turbulence (Bagnold, 1954; Wang

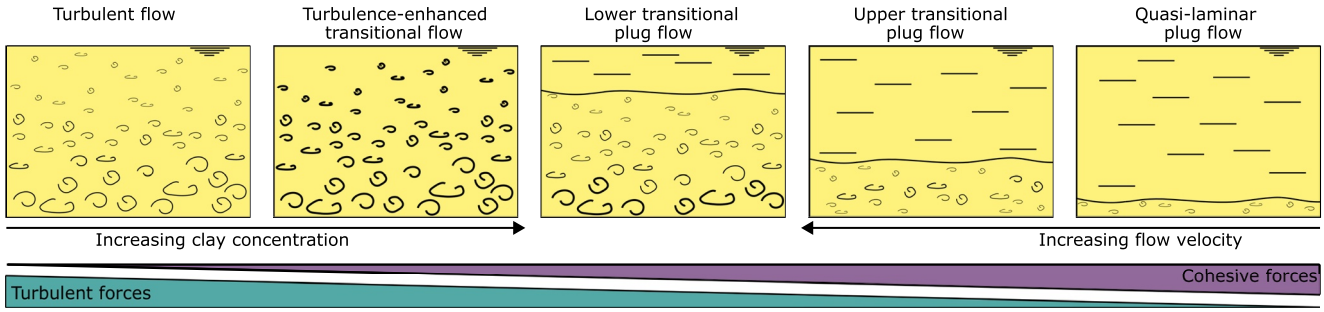

Figure 1. Schematic model of the balance between cohesive and turbulent forces that determines the behavior of turbulent, transitional, and laminar clay-laden flows, divided into five different clay flow types after the classification scheme of Baas et al. (2009). Modified after Baas et al. (2009).

& Larsen, 1994), influencing sediment transport rates and erosion and deposition patterns (Metha et al., 1989; Partheniades, 1965).

Cohesive clay particles may collide and form larger particles, or flocs, when the distance between the particles is sufficiently small (Van Olphen, 1977; Winterwerp and van Kesteren, 2004). Networks of flocs in the flow, that is, clay gels, enhance viscosity and yield stress, and thus are a key control on flow turbulence (Baas & Best, 2002). Research into steady, uniform clay flows indicates a close interaction between turbulent and cohesive forces, controlling the dynamic structure of clay flows (Baas & Best, 2002; Baas et al., 2009). As the clay concentration increases, it becomes increasingly difficult to break the cohesive bonds between particles, resulting in the formation of a pervasive network of permanently interlinked clay particles; turbulent energy is dissipated by the high effective viscosity, and the flow becomes laminar. Conversely, the electrostatic bonds between the clay particles can be broken in regions of high shear. Thus, an increase in turbulence generation in the flows by, for example, an increasing flow velocity has the potential to break bonds between the clay particles and reduce the flow viscosity (Partheniades, 2009). This shifting balance between turbulent and cohesive forces regulates the dynamic structure of cohesive flows (Baas et al., 2009).

Baas et al. (2009) defined a clay flow classification scheme based on flume experiments. The only technique available for velocity measurements in high concentrated flows is Ultrasonic Velocity Profilers, which are designed to work along a single beam. This allows velocity measurements to be collected in one flow direction and consequently, Baas et al. (2009) based the clay flow classification scheme on streamwise velocity measurements instead of a 3D turbulence field. The clay flow classification scheme consists of five different clay flow types in order of increasing clay concentration: turbulent flow, turbulence-enhanced transitional flow, lower transitional plug flow, upper transitional plug flow, and quasi-laminar plug flow (Figure 1). Turbulent flow exhibits a logarithmic velocity profile with an associated decrease in turbulence intensity away from the bed (Nezu & Nakagawa, 1993). The velocity of turbulence-enhanced transitional flows progressively diminishes, in particular close to the base of the flow, accompanied by a progressive increase in turbulence intensity over the full flow depth, whilst the logarithmic velocity profile is maintained. A progressive increase in clay concentration in lower transitional plug flows results in the formation of a plug, which thickens from the water surface downwards. This flow type exhibits a decreased near-bed velocity and increased near-bed turbulence in combination with decreased turbulence intensity in the outer flow. The plug flow further thickens downwards in upper transitional plug flows with increasing clay concentration, whilst the maximum turbulence intensity moves away from the bed and decreases. The upward shift in turbulence production is explained through thickening of the viscous sublayer (Best & Leeder, 1993; Li & Gust, 2000) and the development of an internal shear layer (Baas & Best, 2002), which separates the near-bed region from the plug flow region. Further increasing the clay concentration results in fully suppressed turbulence in quasi-laminar plug flows, apart from minor residual turbulence near the base of the flow in a thin shear layer.

Flows are naturally non-uniform; here, flow non-uniformity is taken to refer to streamwise changes in depth-averaged velocity. The effect of clay on streamwise decelerating and accelerating flow is essential for understanding sediment-laden flow dynamics. The formation of bonds between cohesive sediment particles is a time-dependent (thixotropic) process, and, therefore, cohesive sediment-laden flows need time to adjust to spatial variations in flow velocity. However, the changing balance between turbulent and cohesive forces in

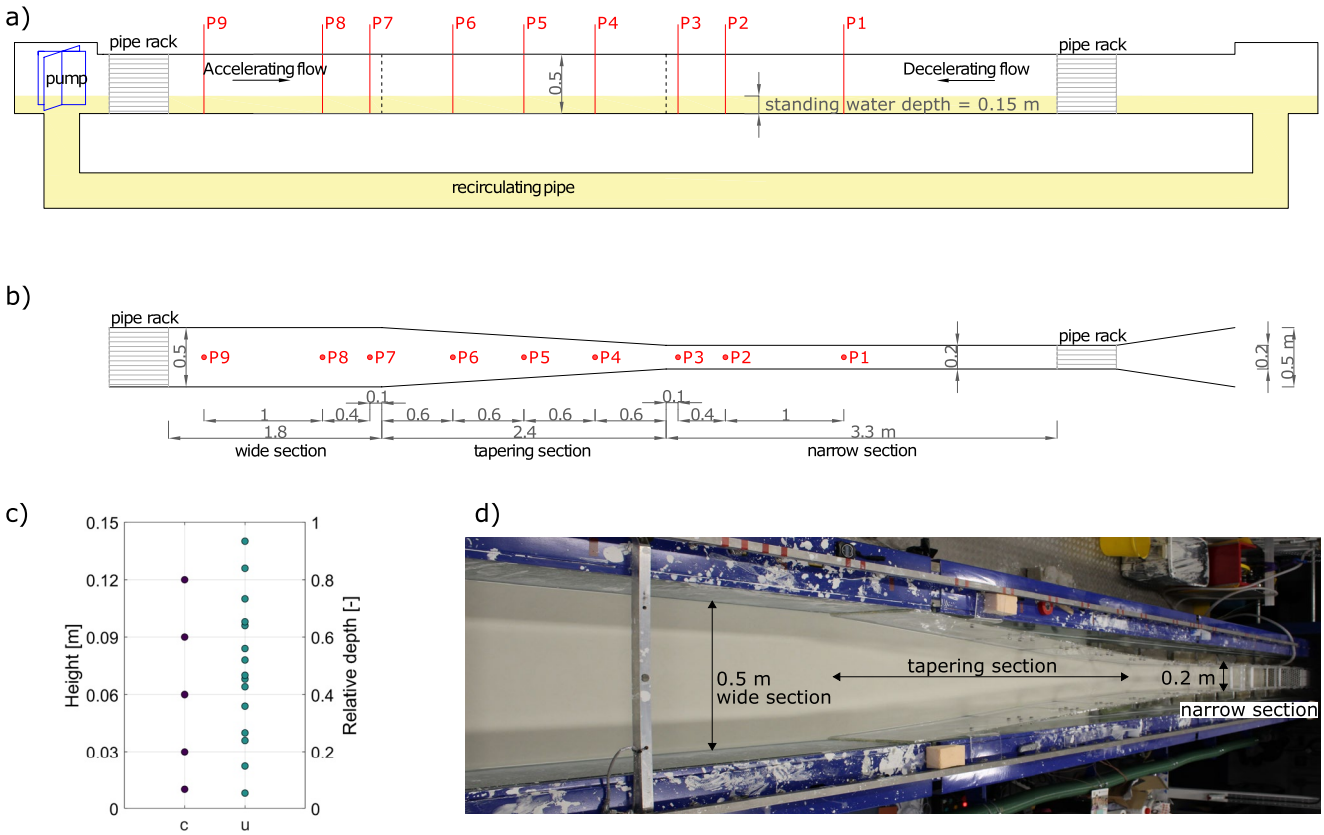

Figure 2. (a) Side view of the experimental setup, (b) top view of the inset channel, with points P indicating measurement locations, (c) velocity (u) and sediment concentration (c) measurement positions above the channel bed; relative depth = height/depth, (d) photo of the flume setup. All dimensions in meters.

clay-laden flows under non-uniform conditions is poorly understood. Understanding this balance is pivotal as erosion, transport, and deposition of sediment depend on the magnitude and distribution of flow turbulence (Dorrell et al., 2018). Spatio-temporal increases and decreases in turbulence directly affect the transport capacity and deposition and erosion patterns (Dorrell & Hogg, 2012; Moody et al., 2013).

An increased understanding of the influence of cohesive sediment on non-uniform flow conditions is needed. This paper details experimental results on the flow structure of clay-laden flows, for the first time isolating the effect of non-uniformity by spatial deceleration and acceleration in open-channel flows. The aim is to understand the adaptation of clay-laden flows to non-uniform flow conditions. We address the following research questions: (a) What are the mean flow and streamwise turbulence characteristics of horizontally decelerating and accelerating clay-laden flows (Section 3)? (b) How do non-uniform flows with different suspended clay concentration compare to each other and to uniform clay-laden flows, that is, which clay flow types can be identified in clay-laden decelerating and accelerating flows (Section 4.1)? (c) How much time do decelerating and accelerating flows need to adapt to the changing flow conditions (Section 4.2)? (d) Are there differences in adaptation between decelerating and accelerating clay-laden flows (Section 4.3)?

2. Methodology

Mixtures of pure kaolinite (Imerys Polwhite-E, median particle size $D_{50} = 9\,\mu m$, sediment density $\rho_s = 2{,}600\,kg\,m^{-3}$) and fresh water were circulated through a horizontal hydraulic flume by means of a variable-discharge slurry pump (Figure 2a). The flume was 10 m long and 0.5 m wide, with a standing water depth, h_0, of 0.15 m. At the upstream end, the flume contained a turbulence-damping grid to straighten the flow. The flow moved over a flat, smooth floor downstream of the turbulence-damping grid. An inset channel was placed in the flume. It had a 0.2 m wide narrow section and a 2.4 m long tapering section. This division in the flume results in a flume expansion or narrowing with a ratio of 1 to 16; this smooth transition avoided flow separation or recirculation cells.

Table 1
Experimental Conditions at Selected Positions in the Flume

Experimental run	Q [m^3/s]	C [vol %]	h_0 [m]	T [^{0}C]	Measuring point	$\overline{\overline{U}}$ [m/s]	Fr [-]	Re [- · 10^4]
Decelerating flow								
D1-C0.0	0.021	0.00	0.150	16.0	P2	0.69	0.57	10.3
					P5	0.52	0.43	7.8
					P8	0.33	0.27	4.9
D2-C0.0	0.015	0.00	0.158	17.6	P2	0.49	0.40	7.8
					P5	0.38	0.30	5.9
					P8	0.28	0.23	4.5
D3-C0.9	0.014	0.92	0.150	18.7	P2	0.48	0.39	6.7
					P5	0.35	0.29	4.9
					P8[a]	0.28	0.23	4.0
D4-C1.5	0.019	1.47	0.150	18.0	P2	0.64	0.53	8.3
					P5	0.45	0.37	6.0
					P8	0.33	0.27	4.3
D5-C2.7	0.016	2.67	0.150	18.0	P2	0.54	0.45	5.8
					P5	0.42	0.35	4.5
					P8	0.27	0.22	2.9
Accelerating flow								
A1-C0.0	0.015	0.00	0.170	17.6	P2	0.45	0.35	7.6
					P5	0.26	0.20	4.4
					P8	0.16	0.13	2.7
A2-C1.4	0.014	1.39	0.170	18.0	P2	0.41	0.32	6.2
					P5	0.26	0.20	3.9
					P8[a]	0.20	0.17	3.0
A3-C1.5	0.016	1.54	0.185	18.7	P2	0.43	0.32	6.9
					P5	0.27	0.20	4.3
					P8[a]	0.20	0.15	2.3
A4-C2.8	0.015	2.77	0.180	18.2	P2	0.41	0.31	5.1
					P5	0.31	0.23	3.8
					P8[a]	0.20	0.15	2.5

Note. Q = discharge, based on velocity measurements at P2 with assumed minimal change in velocity over the flume width; C = spatial-averaged volumetric concentration, based on an average of suspended sediment samples over the depth and along the length of the flume; h_0 = standing water depth at P8; T = water temperature; $\overline{\overline{U}}$ = depth-averaged velocity; Fr = Froude number; Re = Reynolds number. The labeling of experimental runs is defined using D for decelerating and A for accelerating flows and the value of clay concentration.

[a]deposition was observed at this location.

The inset forced the flow through a narrow to wide transition (decelerating flows) or through a wide to narrow transition (accelerating flows) depending on the flow direction (Figure 2b). Thus, in contrast to earlier work in non-tapering flumes (Baas & Best, 2002; Baas et al., 2009), this channel design enabled controlled spatial changes in the flow velocity and turbulence to be measured.

2.1. Experimental Conditions

Table 1 shows the range of clay concentrations and flow velocities used; control experiments were conducted with clear water. Clay was soaked in water for a minimum of 1 day before adding the clay suspension to the flume, to guarantee that no dry clumps remained. To ensure a uniform mixture of clay and water in the flume, initially,

the flume was run at high rotational speed of the slurry pump for 30 min combined with additional mixing in the wide section using a hand-held mixture. Afterward, the flume ran for 16–20 hr to allow the clay-laden flows to reach equilibrium conditions and allow for any deposition of clay before measurements were taken. This allowed the assessment of streamwise turbulence dynamics of non-uniform clay-laden flows without the influence of erosional or depositional processes. Control measurements of the velocity were collected 3 hr after experimental runs to confirm the establishment of equilibrium conditions.

2.2. Data Acquisition

At the start of each run, the water temperature was measured with a thermometer and the water depth was measured with a ruler at P8. A vertical rack of siphon tubes was used to synchronously collect 60 ml samples over a duration of 2 min at five different heights in the water column and at three locations for the decelerating (P3, P5, P9) and accelerating (P1, P5, P7) flows (Figures 2b and 2c). The three locations covered the longest lengths possible in the flume for the development of either decelerating or accelerating flow. Hence, the measurement locations included the first measurement point upstream of the tapering section (P3 for decelerating flow, P7 for accelerating flow), the middle of the tapering section (P5) and the furthest measurement point downstream of the tapering section (P9 for decelerating flow and P1 for accelerating flow). The collected samples were weighed and dried to determine their volumetric clay concentration. The horizontal flow velocity was measured at nine locations along the flume using Ultrasonic Velocity Profilers facing upstream (Figures 2b and 2c) (Best et al., 2001; Takeda, 1991). Ultrasonic Velocity Profilers measure flow velocity using the Doppler shift, which relies on the use of pulsed ultrasound echography. A short emission of ultrasound is transmitted from a profiler, and the same profiler receives the echo reflected from suspended particles in the flow. To determine the flow velocity, the Doppler shift frequency is determined from several repeated ultrasound pulses. In these experiments, five 4 MHz probes were stacked on top of each other with a distance of 14 mm between their centers. The probes collected velocity data for 500 cycles with a 50 ms delay between probes to avoid measurement interference. The probe array was shifted vertically to three different heights during the experiment to cover the full flow depth, resulting in a total of 15 measurement elevations per location (Figure 2c). Depending on the experimental conditions, these settings resulted in measurement durations of 174–330 s at a temporal resolution of 2.9 to 1.5 Hz. Velocity measurements taken at 0.03–0.05 m from the probe head were used in the analysis. An overview of the settings of the Ultrasonic Velocity Profilers used in these experiments is provided in the Supporting Information S1.

2.3. Data Processing

Artificial noise was removed from the velocity signal by eliminating values three standard deviations away from a temporal moving mean measured over 31 datapoints. On average, these spikes accounted for less than 3% of the data. Datapoints were excluded where deposition occurred. The temporal mean flow velocity, $\overline{U}$, and its standard deviation, RMS(u'), were then calculated from the time series of instantaneous velocity data at each measurement height (Baas et al., 2009):

$$\overline{U} = \frac{1}{n}\sum_{i}^{n} u_i \tag{1}$$

$$\mathrm{RMS}\left(u'\right) = \sqrt{\frac{1}{n}\sum_{i}^{n}\left(u_i - \overline{U}\right)^2} \tag{2}$$

where n is the number of velocity measurements. The coefficient of variation is used as a dimensionless measure for turbulence intensity (e.g., Baas et al., 2009):

$$\mathrm{RMS}\left(u'\right)_0 = \frac{\mathrm{RMS}(u')}{\overline{U}} \cdot 100 \tag{3}$$

Depth-averaged velocity was calculated by integrating the time-averaged velocities over the depth. The integral was numerically evaluated; velocities were set to zero at the bed and velocities at the water surface were assumed to have the same value as the first measurement position below that level:

$$\overline{\overline{U}} = \frac{1}{h_0}\int_0^{h_0} \overline{U}\, dz \tag{4}$$

where z is height above the bed. Depth-averaged turbulence intensity was calculated by integrating the turbulence intensity values over the depth.

$$\overline{\mathrm{RMS}(u')_0} = \frac{1}{h_0}\int_0^{h_0} \mathrm{RMS}\left(u'\right)_0 dz \tag{5}$$

On the rare occasion that the reflected signal strength of an Ultrasonic Velocity Profiler is not sufficient to collect accurate velocity measurements, the velocity measurements can result in unexpected strong velocity fluctuations. A moving mean is not guaranteed to remove these errors and a second stage of data cleaning is required. These outliers in the processed velocity data set were excluded as follows. Data was identified as an outlier when either the flow velocity, $\overline{U}$, or its standard deviation RMS(u'), was 40% higher or lower than the median value of the six immediately surrounding measurement points from the nearest upstream and downstream locations:

$$\frac{\left|\mathrm{median}\left(\overline{U}_{j-1,i-1}, \overline{U}_{j,i-1}, \overline{U}_{j+1,i-1}, \overline{U}_{j-1,i+1}, \overline{U}_{j,i+1}, \overline{U}_{j+1,i+1}\right) - \overline{U}_{j,i}\right|}{\overline{U}_{j,i}} \cdot 100 > 40 \tag{6}$$

with i = point, j = height. Here, the median was used to avoid weighting from outliers. At the outer locations, P1 and P9, the points in the narrow (P2 and P3) or wide (P7 and P8) section were used to include a sufficient number of measurement points in the determination of the median, for example, for outer location P1:

$$\frac{\left|\mathrm{median}\left(\overline{U}_{j-1,P2}, \overline{U}_{j,P2}, \overline{U}_{j+1,P2}, \overline{U}_{j-1,P3}, \overline{U}_{j,P3}, \overline{U}_{j+1,P3}\right) - \overline{U}_{j,P1}\right|}{\overline{U}_{j,P1}} \cdot 100 > 40 \tag{7}$$

Near the bed, larger changes in $\overline{U}$ and RMS(u') are likely and therefore, the lowest measurement elevation was excluded from this outlier analysis. To make sure no outliers are left near the bed, the lowest measurement elevation was compared only to the nearest upstream and downstream locations at the lowest measurement elevation. The second stage of data cleaning, discarded as little as 1% and up to 7% of the datapoints from an experimental data set. To maintain enough datapoints over the depth, the full measurement location (P1–P9) was deemed invalid if >50% of the data were classified as outliers over the full flow depth. The bed height, z_b, was defined as the lowest valid measurement elevation. To compare the same elevation in different flows, the flows are plotted against normalized height adjusted to the deposit level.

$$\tilde{z} = (z - z_b)/h_0 \tag{8}$$

Following Wan (1982), the dynamic viscosity, $\eta\left[N/\left(s/m^2\right)\right]$, of the suspensions was estimated from the measured suspended sediment concentration:

$$\eta = 0.001 + 0.206\left(\frac{C}{100}\right)^{1.68} \tag{9}$$

Then, the Reynolds number was calculated as follows:

$$Re = \frac{\overline{\overline{U}}h_0}{\nu_e} \tag{10}$$

where, the effective viscosity of the suspension, ν_e, was calculated from the ratio of dynamic viscosity over the density of the clay suspension, ρ_m:

$$\nu_e = \eta/\rho_m \tag{11}$$

The identified adaptation length, L, and time scales, T, are calculated in dimensionless form with the standing water depth as characteristic length scale and the discharge as characteristic time scale, for which the velocity at P2 is representative.

$$L = l/h_0\,[-] \tag{12}$$

$$T = t \cdot h_0/U_{P2}\,[-] \tag{13}$$

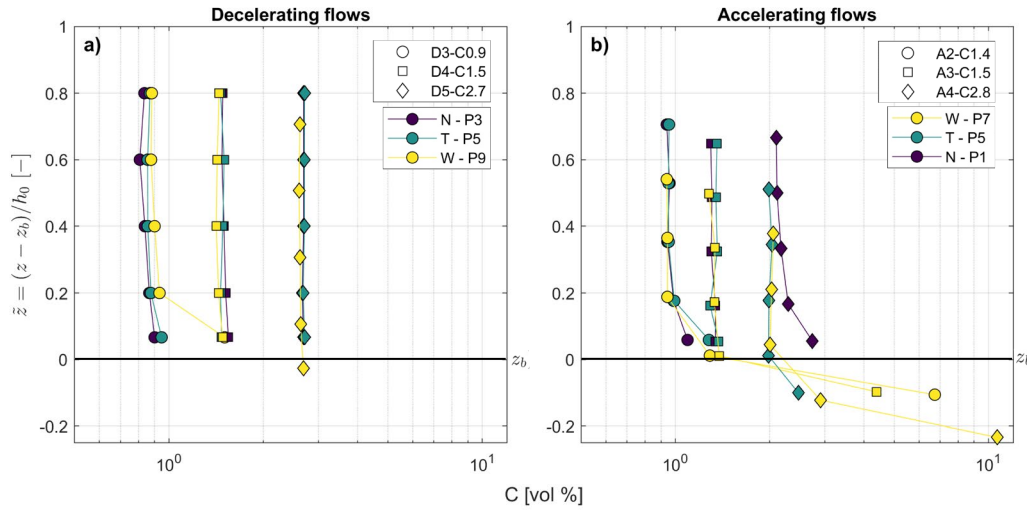

Figure 3. Vertical profiles of volumetric sediment concentration against normalized bed height adjusted to the deposit (Equation 8) for the (a) decelerating and (b) accelerating clay-laden flows. The measurement locations are indicated in the order of the flow direction, where *N*, *T*, and *W* denote narrow, tapering, and wide sections, respectively.

where l is the identified adaptation length in the flume and t is the identified adaptation time in the flume.

3. Results

The results section provides an overview of the collected measurements. This includes suspended sediment concentrations (Section 3.1) and streamwise velocity and turbulence intensity profiles along the flume for decelerating flows (Section 3.2) and accelerating flows (Section 3.3).

3.1. Clay Concentration

The suspended sediment concentrations for the decelerating flows were nearly uniform over the flow depth (Figure 3a). The exception is run D3-C0.9, which contained a higher clay concentration at the lowest sampling point in the wide section (P9) of the flume. This may be explained as D3-C0.9 has the slowest recorded velocity at P9, of the decelerating flows, and thus the greatest likelihood for deposition from the suspension of the cohesive sediment (Figure 5a). The suspended sediment concentrations for the accelerating flows were non-uniform over the flow depth, with higher near-bed sediment concentrations, particularly in the wide section of the flume (Figure 3b). These higher concentrations were in the deposit level of the flows ($\tilde{z} < 0$).

3.2. Decelerating Flows

3.2.1. Clear Water Flows

Figure 4a shows the time-averaged streamwise velocity profiles ($\overline{U}$) and the depth-averaged velocity magnitudes ($\overline{\overline{U}}$) along the flume for the decelerating clear-water flow D1-C0.0. Upstream, in the narrow section of the flume (P1 to P3; Figure 2b), the depth-averaged velocity shows that the flow is nearly uniform. The velocity decreases progressively as the width of the flume increases (P4 to P6) and continues to decrease more gradually in the wide section of the flume (P7 to P9). At the end of the flume (P9), uniform conditions are established in the lower half of the flow, but they are not fully established in the upper half. Figure 4b shows the velocities along the flume for the lower-discharge decelerating flow D2-C0.0 (Table 1). The depth-averaged velocities show a comparable pattern to flow D1-C0.0 (Figures 4a and 4b).

Figures 4c and 4d show the time-averaged streamwise turbulence intensity profiles ($\mathrm{RMS}(u')_0$) and the depth-averaged turbulence intensities ($\overline{\mathrm{RMS}(u')_0}$) along the flume for D1-C0.0 and D2-C0.0, respectively. The depth-averaged turbulence intensity values of both flows are nearly uniform in the narrow section (P1 to P3). The turbulence intensities decrease away from the bed in the narrow section (Figures 4c and 4d). As the velocity

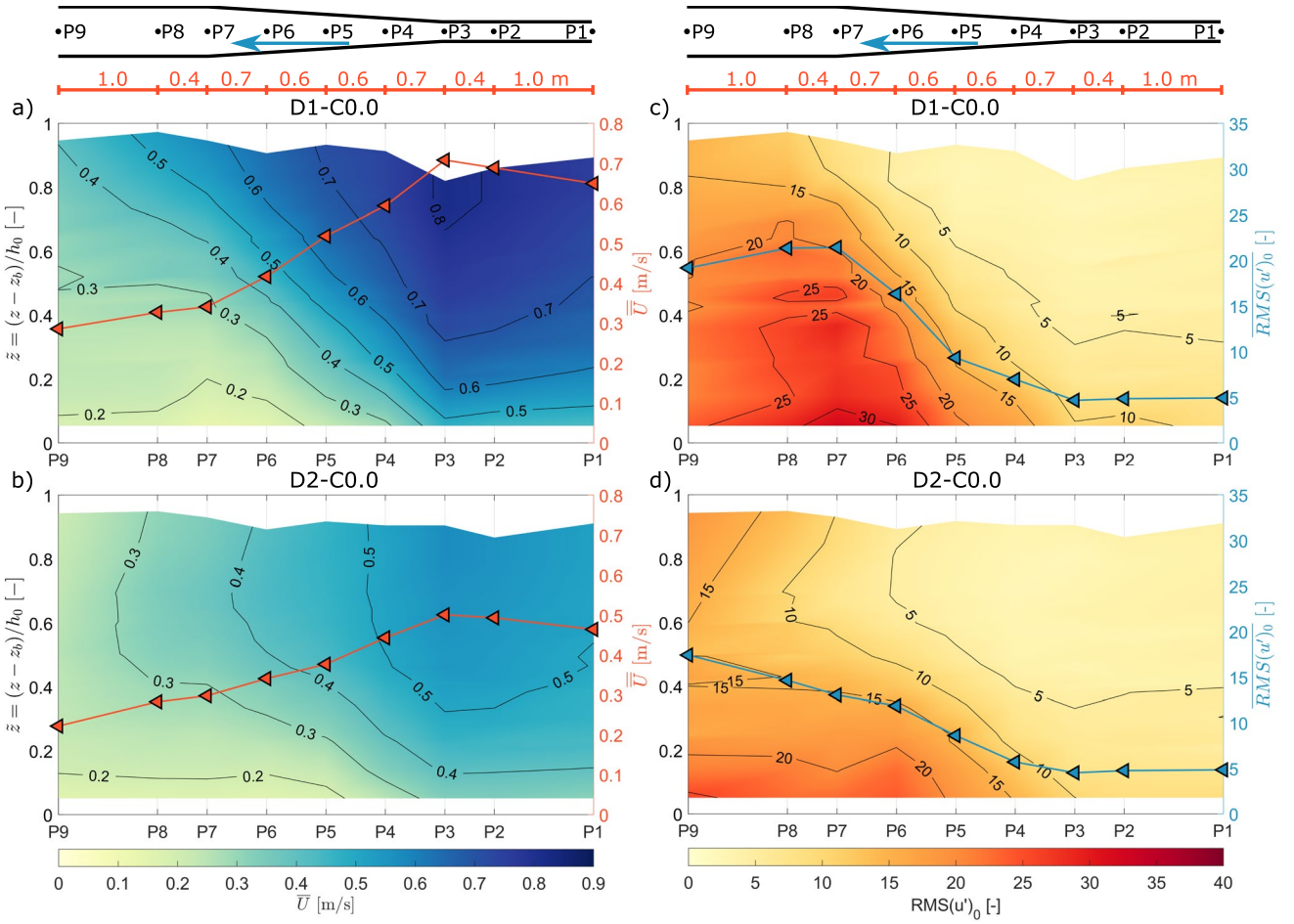

Figure 4. Depth-averaged velocity magnitudes ($\overline{U}$) and time-averaged streamwise velocity profiles ($\overline{U}$) along the flume for the decelerating clear water flows (a) D1-C0.0 and (b) D2-C0.0. Depth-averaged turbulence intensities ($\overline{\text{RMS}(u')_0}$) and time-averaged streamwise turbulence intensity profiles ($\text{RMS}(u')_0$) along the flume for flows (c) D1-C0.0 and (d) D2-C0.0.

decreases in the widening section (P4 to P6), turbulence intensity increases near the bed, while also progressively increasing upward in the flow downstream. In both flows, this results in an increase in the vertical gradient of turbulence intensity in the widening section followed by a decrease in the vertical gradient in the wide section. The depth-averaged turbulence intensity at P9 is 4.0 times higher than at P2 for D1-C0.0 (Figure 4c) and 3.7 times higher for D2-C0.0 (Figure 4d), despite the decrease in velocity. Similar increases in turbulence intensity have been observed before in clear water decelerating flows (Kironoto & Graf, 1995; Qingyang, 2009). Toward the end of the wide section, at P9, the turbulence intensities remain non-uniform, suggesting that the length of the flume is insufficient to establish equilibrium after the widening section.

3.2.2. Clay-Laden Flows

Figures 5a–5c show the time-averaged streamwise velocity profiles ($\overline{U}$) and the depth-averaged velocity magnitudes ($\overline{\overline{U}}$) along the flume for the clay-laden decelerating flows D3-C0.9, D4-C1.5, and D5-C2.7, respectively. Figures 5d–5f show the time-averaged streamwise turbulence intensity profiles ($\text{RMS}(u')_0$) and the depth-averaged turbulence intensities ($\overline{\text{RMS}(u')_0}$) along the flume for the same flows. In the narrow section (P1 to P3), the depth-averaged velocities are nearly uniform for each decelerating clay-laden flow. The depth-averaged velocities for each flow decrease along the widening section similarly, albeit with a slightly higher rate of decrease for flow D4-C1.5. In the wide section (P7 to P9), the depth-averaged velocities are lowest and nearly uniform.

The depth-averaged turbulence intensity values are nearly uniform in the narrow section (P1 to P3) (Figures 5d–5f); the turbulence intensities decrease away from the bed. As the velocity decreases in the widening section (P4 to

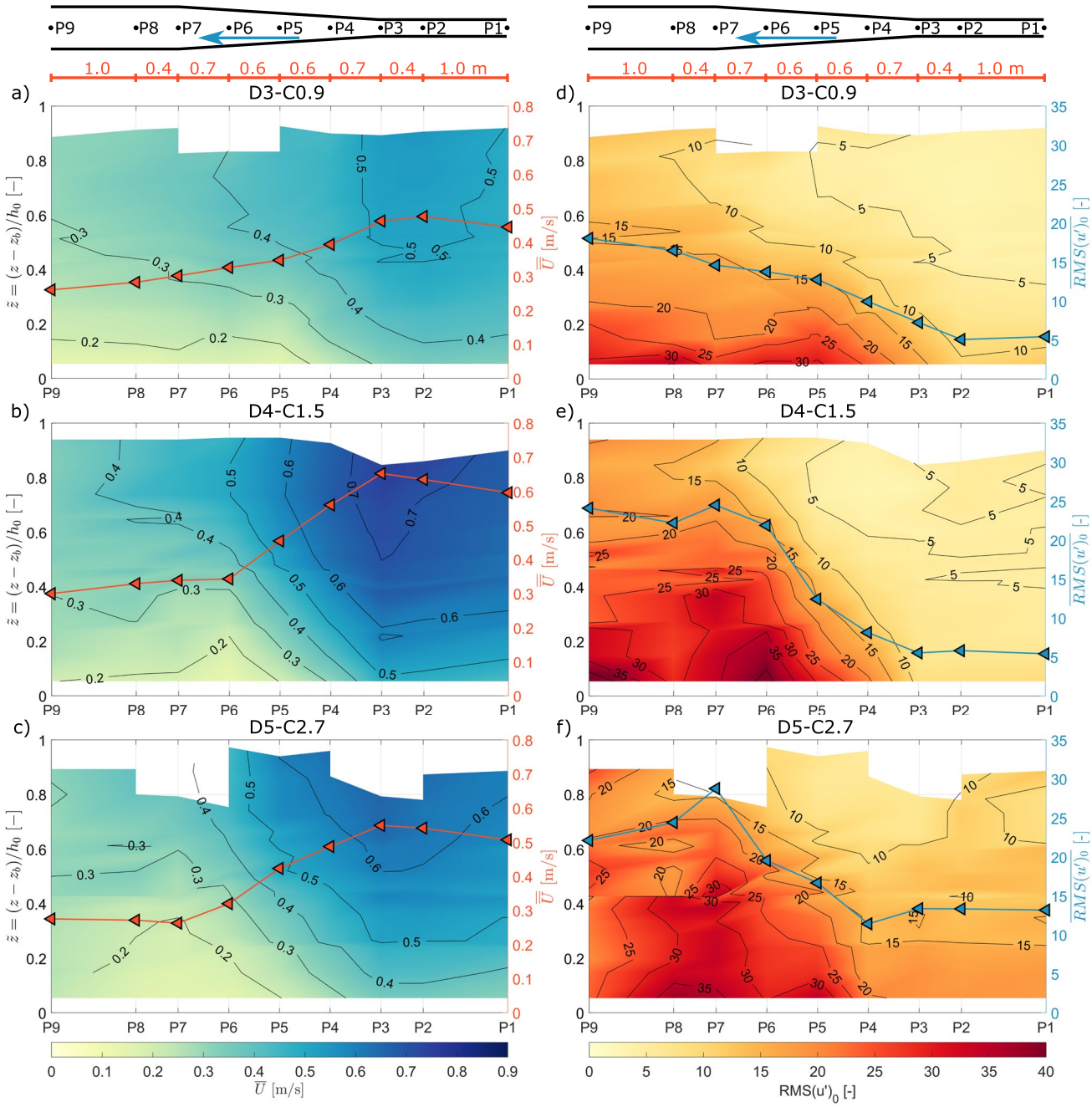

Figure 5. Depth-averaged velocity magnitudes ($\overline{U}$) and time-averaged streamwise velocity profiles ($\overline{U}$) along the flume for the decelerating clay-laden flows (a) D3-C0.9, (b) D4-C1.5, and (c) D5-C2.7. Depth-averaged turbulence intensities ($\overline{\mathrm{RMS}(u')_0}$) and time-averaged streamwise turbulence intensity profiles ($\mathrm{RMS}(u')_0$) along the flume for flows (d) D3-C0.9, (e) D4-C1.5, and (f) D5-C2.7.

P6), the turbulence intensity increases, initially near the bed, and then progressively higher in the flow downstream. This results in an increase in the vertical gradient of turbulence intensity in the widening section followed by a decrease in vertical gradient into the wide section. Towards the end of the wide section, at P9, the turbulence intensity shows a steep vertical gradient for flows D3-C0.9 and D4-C1.5. The turbulence intensity for flow D5-C2.7 remains high between P7 and P9. Despite the decrease in velocity, the depth-averaged turbulence intensity at P9 is 3.6 times higher than at P2 for D3-C0.9, 4.3 times higher for D4-C1.5 and 1.8 times higher for D5-C2.7. Towards the end of the wide section, at P9, the turbulence intensities remain non-uniform, suggesting that the length of the flume is insufficient to establish equilibrium after the widening section. Despite both

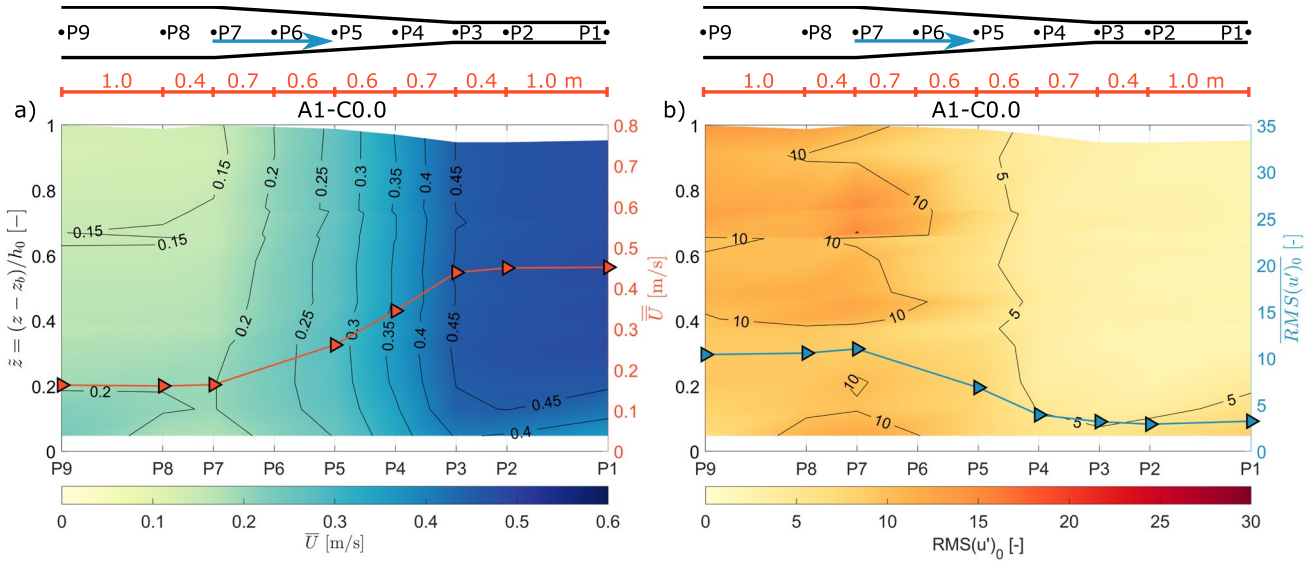

Figure 6. (a) Depth-averaged velocity magnitudes ($\overline{\overline{U}}$) and time-averaged streamwise velocity profiles ($\overline{U}$) along the flume for the accelerating clear water flow A1-C0.0. (b) Depth-averaged turbulence intensities ($\overline{\mathrm{RMS}(u')_0}$) and time-averaged streamwise turbulence intensity profiles ($\mathrm{RMS}(u')_0$) along the flume for flow A1-C0.0.

the clear water and clay-laden decelerating flows not reaching equilibrium flow conditions in the wide section, distinct differences in patterns of increase in turbulence intensity can be identified, which determines clay flow type, discussed below in Section 4.1.

3.3. Accelerating Flows

The flow direction was reversed to achieve accelerating conditions, so the flow direction was from left to right, that is, from P9 to P1 (cf. Figures 2a and 2b).

3.3.1. Clear Water Flows

Figure 6a shows the time-averaged streamwise velocity profile ($\overline{U}$) and the depth-averaged velocity magnitude ($\overline{\overline{U}}$) along the flume for the accelerating clear-water flow A1-C0.0. Upstream, in the wide section of the flume (P9 to P7; Figure 2b), the depth-averaged velocity shows that the flow is nearly uniform. The flow accelerates progressively as the width of the flume decreases (P6 to P4) and nearly uniform flow re-establishes in the narrow section (P3 to P1).

Figure 6b shows the time-averaged streamwise turbulence intensity profile ($\mathrm{RMS}(u')_0$) and the depth-averaged turbulence intensities ($\overline{\mathrm{RMS}(u')_0}$) along the flume for flow A1-C0.0. The depth-averaged turbulence intensity values are nearly uniform in the wide section (P9 to P7). The turbulence intensity values decrease as the velocity increases in the narrowing section (P6 to P4) and remain nearly uniform in the narrow section (P3 to P1). The depth-averaged turbulence intensity at P1 is lower by a factor of 0.3 than at P8. The velocity increases toward the narrow section, but its standard deviation ($\mathrm{RMS}(u')$) does not rise accordingly, which results in a decrease in turbulence intensity ($\mathrm{RMS}(u')_0$). Similar decreases in turbulence intensity have been observed before in accelerating clear water flows (Cardoso et al., 1991).

3.3.2. Clay-Laden Flows

Figures 7a–7c show the time-averaged streamwise velocity profiles ($\overline{U}$) and the depth-averaged velocity magnitudes ($\overline{\overline{U}}$) along the flume for the clay-laden accelerating flows A2-C1.4, A3-C1.5, and A4-C2.8, respectively. Figures 7d–7f show the time-averaged streamwise turbulence intensity profiles ($\mathrm{RMS}(u')_0$) and the depth-averaged turbulence intensities ($\overline{\mathrm{RMS}(u')_0}$) along the flume for the same flows. Upstream in the wide section (P9 to P7; Figure 2b), the depth-averaged velocity shows that the flow is nearly uniform. The flow accelerates progressively

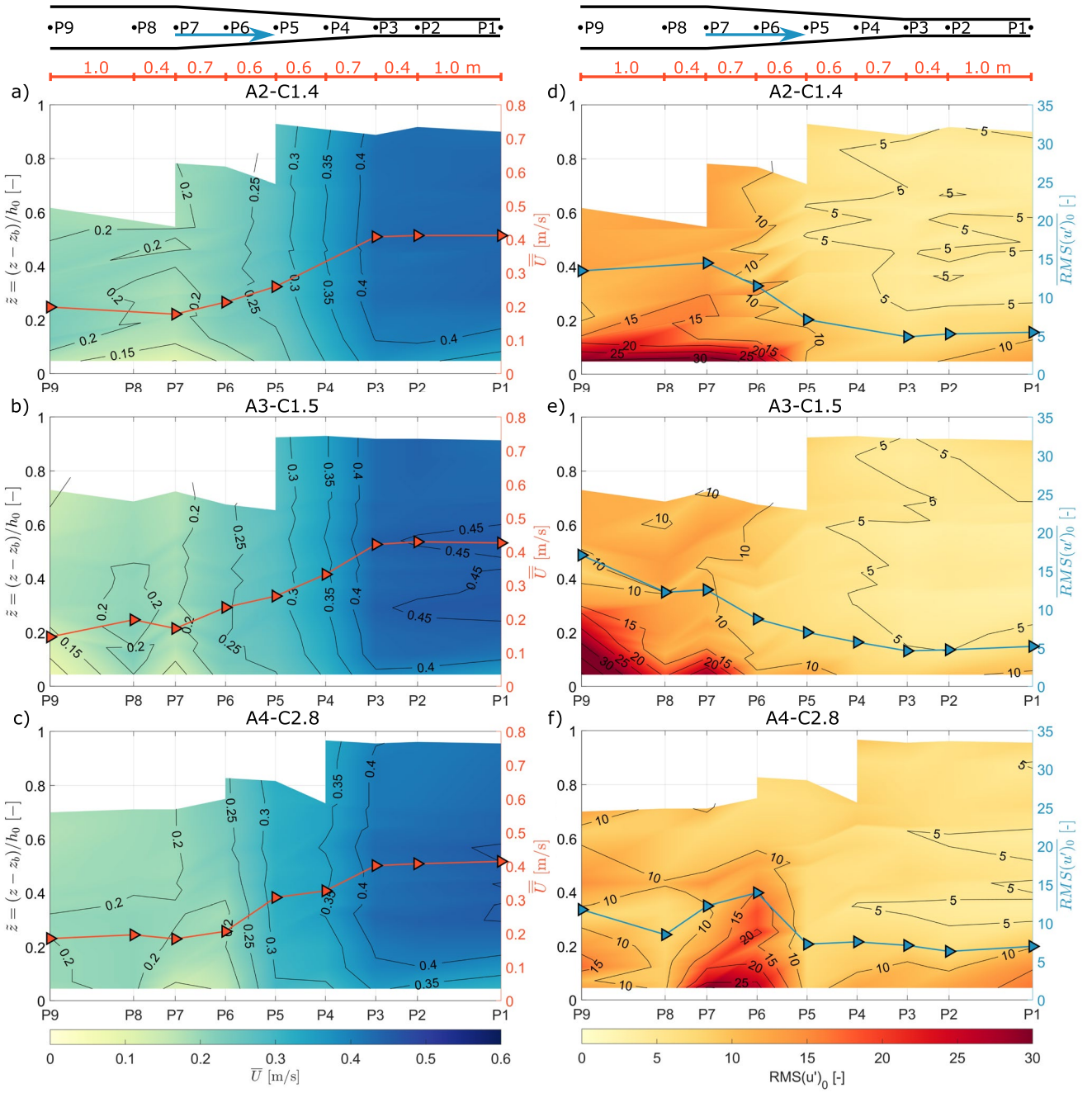

Figure 7. Depth-averaged velocity magnitudes ($\overline{\overline{U}}$) and time-averaged streamwise velocity profiles ($\overline{U}$) along the flume for the accelerating clay-laden flows (a) A2-C1.4, (b) A3-C1.5, and (c) A4-C2.8. Depth-averaged turbulence intensities ($\overline{\mathrm{RMS}(u')_0}$) and time-averaged streamwise turbulence intensity profiles ($\mathrm{RMS}(u')_0$) along the flume for flows (d) A2-C1.4, (e) A3-C1.5, and (f) A4-C2.8.

as the width of the flume decreases (P6 to P4) and nearly uniform flow re-establishes in the narrow section (P3 to P1).

In the wide section (P9 to P7), where the velocity is low, the depth-averaged turbulence intensities of all three clay flows are higher than in the narrowing and narrow sections, where the velocities are higher (Figures 7d–7f). Toward the base of the flow, the turbulence intensity shows a steep vertical gradient in the wide section, with especially high turbulence intensity toward the base of flows A2-C1.4 and A3-C1.5. Notably, the turbulence intensity in the bottom half of the flow at P9 and P8 in the wide section of the flume is lower for flow A4-C2.8

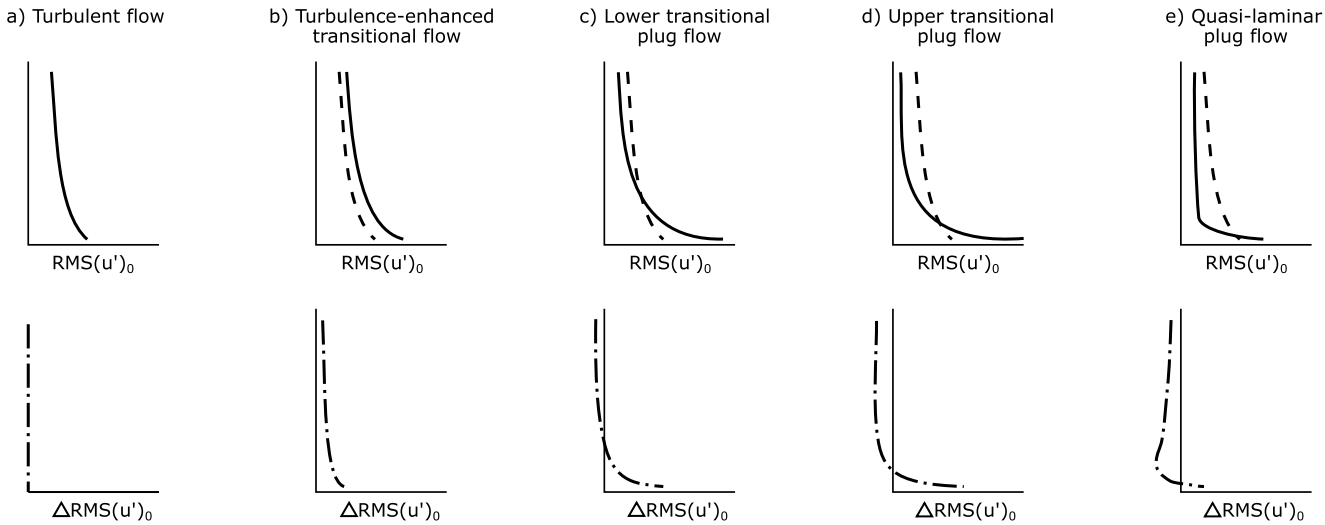

Figure 8. Upper row: schematic model of turbulence intensity profiles ($RMS(u')_0$), divided into five different clay flow types after the classification scheme of Baas et al. (2009), where the dashed line in b-e indicates the turbulence intensity profile for turbulent flow. Lower row: schematic model of the difference in time-averaged streamwise turbulence intensity profiles ($\Delta RMS(u')_0$) between clay flow types and clear water turbulent flows.

(Figure 7f) than for flows A2-C1.4 (Figure 7d) and A3-C1.5 (Figure 7e). The turbulence intensity values are high around P7 for flow A4-C2.8. The depth-averaged turbulence intensity values for all three flows decrease as the velocity increases in the narrowing section (P6 to P4) and remain nearly uniform in the narrow section (P3 to P1). The depth-averaged turbulence intensity at P1 is 0.4 times the intensity at P8 for A2-C1.4, 0.4 times for A3-C1.5 and 0.8 times for A4-C2.8.

4. Discussion

The discussion includes the interpretation of downstream changes in clay flow types in the experimental runs (Section 4.1). Based on the distance between the different clay flow types in the flume, the length scale of the adaptation of clay flows is assessed in Section 4.2. The length scales of decelerating and accelerating clay-laden flows are compared and further implications of the present study are discussed in Section 4.3.

4.1. Clay Flow Types

To determine the clay flow types at the nine measurement locations along the flume initially without influences of flow deceleration or acceleration, the difference in turbulence intensity is assessed between clay-laden flows and clear water flows. Figure 8 shows the profiles of turbulence intensity ($RMS(u')_0$) for the five clay flow types identified by Baas et al. (2009) with an added dashed line indicating the turbulence intensity profile of a clear water turbulent flow. Additionally, Figure 8 shows the difference profiles of turbulence intensity ($\Delta RMS(u')_0$) between the five clay flow types and clear water turbulent flow. When compared with turbulent clear water flow, the difference in turbulence intensity is negligible if the clay-laden flow is classified as turbulent flow. Turbulence-enhanced transitional flows show higher turbulence intensity over the full flow depth and thus, if compared with turbulent flow, the difference profile ($\Delta RMS(u')_0$) results in positive values over the full flow depth. The plug flow formation below the surface for lower transitional plug flows results in negative $\Delta RMS(u')_0$ values below the surface in the difference profile. However, increased $\Delta RMS(u')_0$ values are found near the bed, since lower transitional plug flow exhibits increased near-bed turbulence. With the thickening of the plug flow in upper transitional plug flows, negative $\Delta RMS(u')_0$ values expand toward the bed. Fully suppressed turbulence in quasi-laminar plug flows results in a negative difference profile over most of the flow depth.

Figures 9a and 9b show the difference in time-averaged streamwise turbulence intensity profiles ($\Delta RMS(u')_0$) and in depth-averaged turbulence intensities ($\Delta\overline{RMS(u')_0}$) along the flume for decelerating flows D3-C0.9 and D5-C2.7 versus flow D2-C0.0 and Table 2 shows an overview of the identified clay-flow types. Differences between the normalized turbulence intensity, $RMS(u')_0$, over the normalized flow depth, $\tilde{z}$, allows the assessment

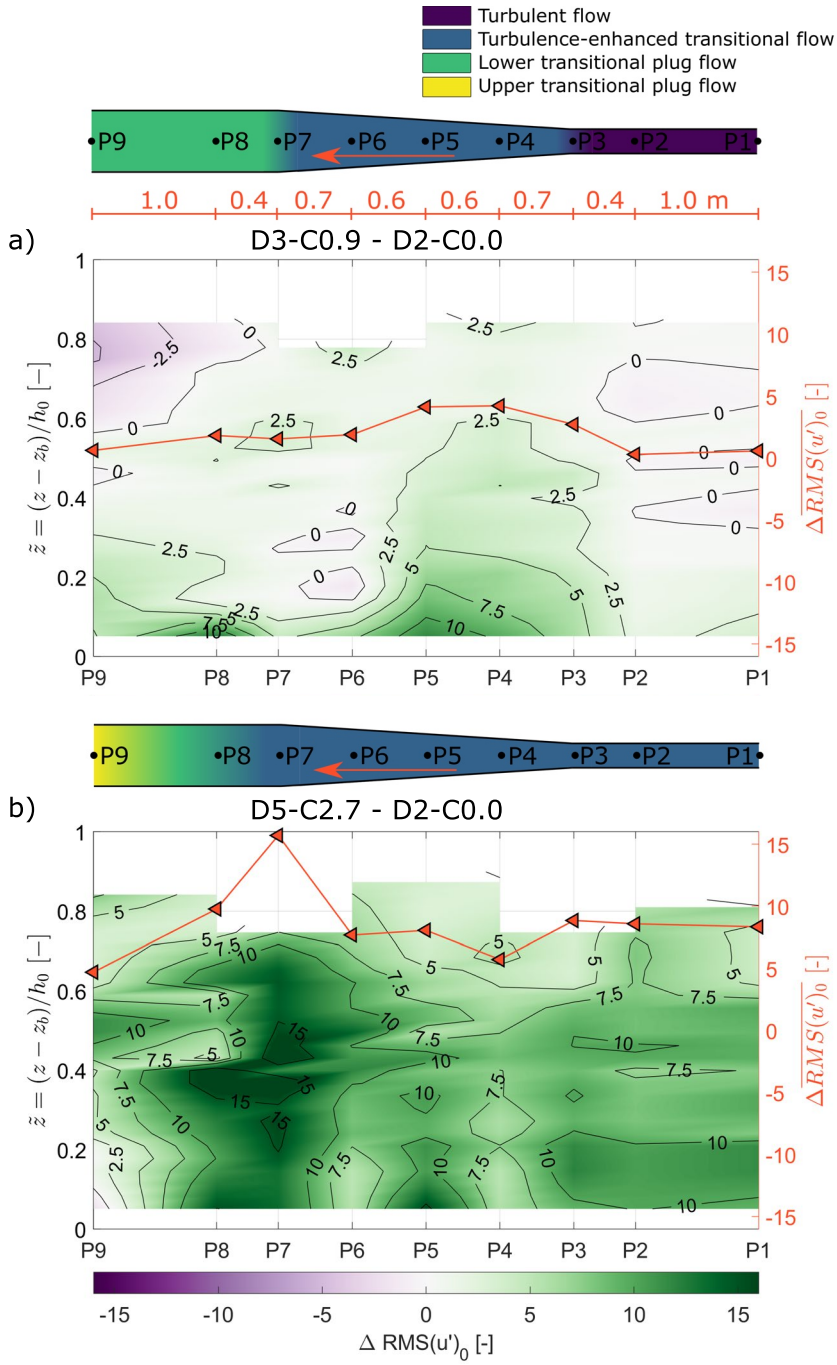

Figure 9. Difference in depth-averaged turbulence intensities ($\Delta\overline{\mathrm{RMS}(u')_0}$) and time-averaged streamwise turbulence intensity profiles ($\Delta\mathrm{RMS}(u')_0$) along the flume for decelerating flows (a) D3-C0.9 minus D2-C0.0 and (b) D5-C2.7 minus D2-C0.0.

of relative influence of clay concentration on non-uniform decelerating flow conditions and the interpretation of clay flow types. Since the relative influence of clay concentration is assessed on the flow dynamics, the same flow types can be identified by comparison of the decelerating clay-laden flows between either clear water flows (D1-C0.0 and D2-C0.0). Here, flow D2-C0.0 is selected for the comparison, because the depth-averaged velocity in the narrow section (P2) before decelerating the flow is more comparable to flow D3-C0.9 and D5-C2.7 (Table 1). Upstream, in the narrow section (P1 to P3; Figure 2b), the turbulence intensity values of flow D3-C0.9 are comparable with the clear-water flow D2-C0.0, that is, the $\Delta\mathrm{RMS}(u')_0$ values are relatively close to zero.

Table 2
Identified Clay Flow Types at the Measurement Positions in the Flume, P9 to P1

	Clay flow type								
Experimental run	P9	P8	P7	P6	P5	P4	P3	P2	P1
Decelerating flow									
D3-C0.9	LTPF	LTPF	LTPF	TETF	TETF	TETF	TF	TF	TF
D5-C2.7	UTPF	LTPF	TETF	TETF	TETF	TETF	TETF	TETF	TETF
Accelerating flow									
A2-C1.4	LTPF	LFTP	LTPF	LTPF	TETF	TETF	TETF	TETF	TETF
A4-C2.8	UTPF	UTPF	LTPF	LTPF	LTPF	TETF	TETF	TETF	TETF

Note. The labeling of the clay flow types in the table is as follows: TF = Turbulent flow; TETF = Turbulence-enhanced transitional flow; LTPF = Lower transitional plug flow; UTPF = Upper transitional plug flow; QLPF = Quasi-laminar plug flow.

This suggests turbulent flow, unaffected by the presence of the suspended clay (Figure 8; Table 2). As the flow decelerates in the widening section (P4 to P6), the $\Delta\mathrm{RMS}(u')_0$ values increase to 10 in the lower half of the flow and to 2.5 in the upper half of the flow. This is typical of turbulence-enhanced transitional flow (Figure 8; Baas et al., 2009); under these conditions, the presence of the clay is inferred to cause a thickening of the viscous sublayer and the development of an internal shear layer with associated enhancement of turbulence (Baas & Best, 2002; Best & Leeder, 1993; Li & Gust, 2000). In the wide section (P7 to P9), the $\Delta\mathrm{RMS}(u')_0$ values remain above zero in the bottom half of flow D3-C0.9 and they are zero or below zero in the top half of the flow. These negative $\Delta\mathrm{RMS}(u')_0$ values suggest the onset of plug development in flow D3-C0.9, that is, lower transitional plug flow (Figure 8; Baas et al., 2009). Flows D3-C0.9 and D4-C1.4 show comparable $\Delta\mathrm{RMS}(u')_0$ patterns (Figures 5d and 5e), such that the same flow types can be identified.

In the narrow section (P1 to P3), the increased clay concentration in flow D5-C2.7 is inferred to cause the observed positive $\Delta\mathrm{RMS}(u')_0$ values (Figure 9b). This suggests that flow D5-C2.7 begins as a turbulence-enhanced transitional flow (Figure 8; Table 2; Baas & Best, 2002). The $\Delta\mathrm{RMS}(u')_0$ values progressively increase through the widening section and beyond, suggesting the development of stronger turbulence-enhanced transitional flow (Baas et al., 2009). While the mean velocity profile of flow D5-C2.7 appears reliable, the heterogeneous vertical pattern of $\Delta\mathrm{RMS}(u')_0$ above a relative depth of 0.4 at position P9 (Figure 9b) may arise from artifacts in the $\mathrm{RMS}(u')$ measurements of this flow. This hinders a reliable inference of flow type at this location, but the decrease in $\Delta\mathrm{RMS}(u')_0$ below the relative depth of 0.4 between P8 and P9 combined with a decrease in $\Delta\mathrm{RMS}(u')_0$ near the top of the flow between P8 and P7 may indicate a change from turbulence-enhanced transitional flow via lower transitional plug flow to upper-transitional plug flow in the wide section (P7 to P9).

Figures 10a and 10b show the difference in time-averaged streamwise turbulence intensity profiles ($\Delta\mathrm{RMS}(u')_0$) and in depth-averaged turbulence intensities ($\Delta\overline{\mathrm{RMS}(u')_0}$) along the flume for accelerating flows A2-C1.4 and A4-C2.8 versus flow A1-C0.0, and Table 2 shows an overview of the identified clay-flow types. Differences between the normalized turbulence intensity, $\mathrm{RMS}(u')_0$ over the normalized flow depth $\tilde{z}$ allows the assessment of relative influence of clay concentration on non-uniform accelerating flow conditions and the interpretation of clay flow types. Upstream, in the wide section and at the start of the narrowing section (P9 to P6), $\Delta\mathrm{RMS}(u')_0$ values are relatively close to zero in the upper half of the flow and increase downwards to 15 in the lower half of flow A2-C1.4. The high near-bed $\Delta\mathrm{RMS}(u')_0$ values, in combination with the low values in the upper half of the flow, are typical of lower transitional plug flow (Figure 8; Baas et al., 2009). As the flow accelerates through the narrowing section (P6 to P4), the near bed $\Delta\mathrm{RMS}(u')_0$ values progressively decrease from 10 to c. 2.5. In the narrow section (P3 to P1), the absolute turbulence intensity values of flow A2-C1.4 are low (Figure 7d), but the $\Delta\mathrm{RMS}(u')_0$ values are increased to around 2.5. This enhanced turbulence intensity suggests weakly turbulence-enhanced or turbulent flow (Figure 8). Flow A3-C1.5 shows comparable turbulence intensity patterns and values (Figures 7d and 7e) and similar flow types can be identified.

Upstream, in the wide section (P9 to P8), $\Delta\mathrm{RMS}(u')_0$ values are up to 2.5 in the lower half of the flow and down to −2.5 in the upper half for flow A4-C2.8 (Figure 10b). This profile suggests upper transitional plug flow, where

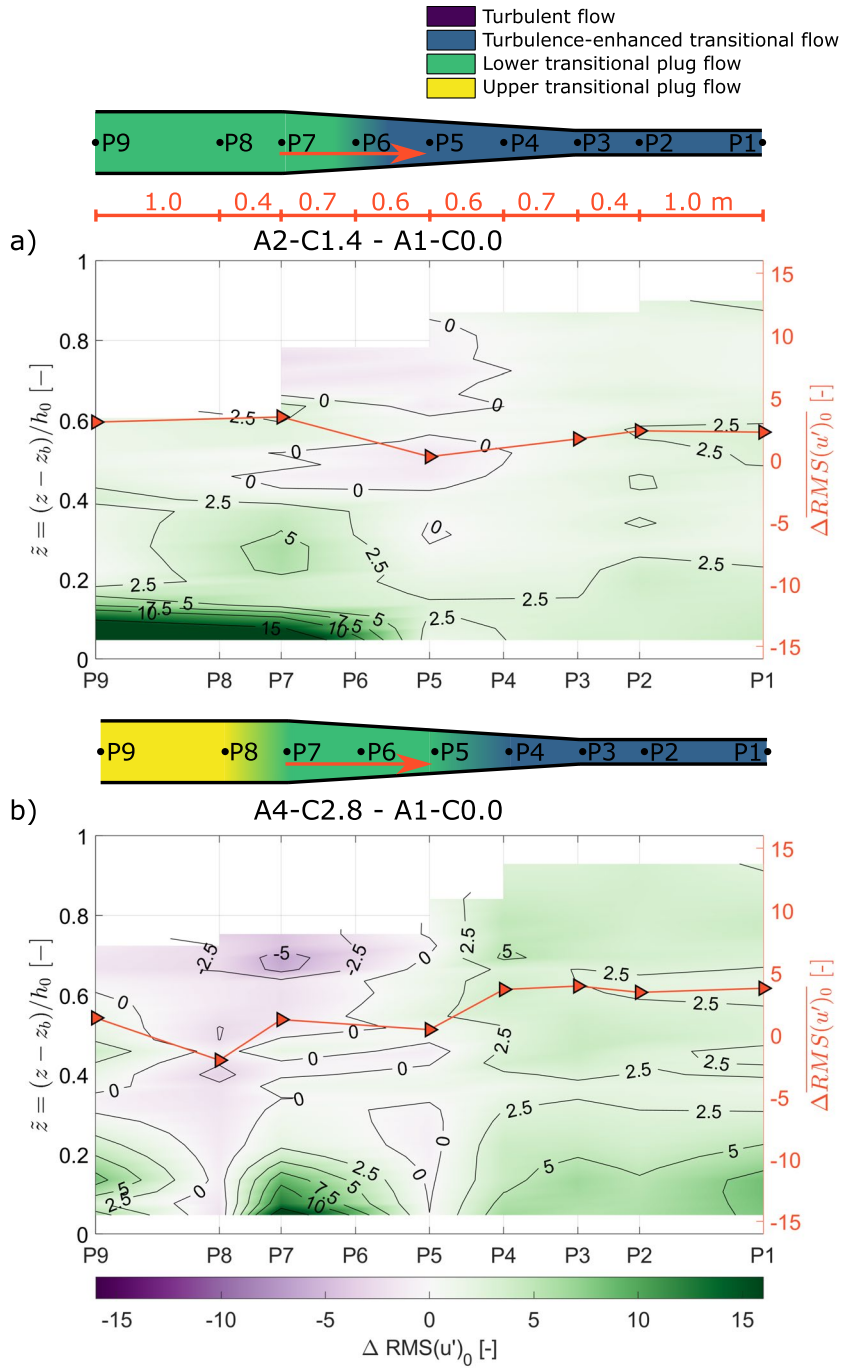

Figure 10. Difference in depth-averaged turbulence intensities ($\Delta\overline{\mathrm{RMS}(u')_0}$) and time-averaged streamwise turbulence intensity profiles ($\Delta\mathrm{RMS}(u')_0$) along the flume for decelerating flows (a) A2-C1.4 minus A1-C0.0 and (b) A4-C2.8 minus A1-C0.0.

turbulence enhancement near the bed is lower than for lower transitional plug flows (Figure 8; cf., flow A2-C1.4 in Figure 10a). Similar to flow A2-C1.4, $\Delta\mathrm{RMS}(u')_0$ values of flow A4-C2.8 between P7 and P6 are relatively close to or below zero in the upper half of the flow and are as high as 15 in the lower half of the flow, suggesting lower transitional plug flow (Figure 10b). Between P4 and P1, the depth-averaged $\Delta\mathrm{RMS}(u')_0$ values are between 2.5 and 5 and vertical $\Delta\mathrm{RMS}(u')_0$ profiles are strictly positive, suggesting turbulence-enhanced transitional flow (Figure 8).

Table 3
Observed Dimensional and Calculated Dimensionless Adaptation Length Scales, l and L, and Time Scales, t and T

Experimental run	Location	Point(s) included in adaptation	Flow regimes	l [m]	L [-]	t [s]	T [-]
Decelerating flow							
D3-C0.9	Widening section	P3	Turbulent flow to turbulence-enhanced transitional flow	0	0	0	0
	Wide section	P7 to P9	Turbulence-enhanced transitional flow to lower transitional plug flow	≥1.4	9.3	≥5.0	2.1
D5-C2.7	Widening section	P3 to P4	Weak to strong turbulence-enhanced transitional flow	0.7	4.7	1.4	0.4
	Wide section	P7 to P9	Turbulence-enhanced transitional flow to upper transitional plug flow	≥1.4	9.3	≥5.2	1.4
Accelerating flow							
A2-C1.4	Narrowing section	P6 to P5	Lower transitional plug flow to turbulence-enhanced transitional flow	0.6	3.5	2.3	0.9
	Narrow section	P3	Uniform turbulence-enhanced transitional flow	0	0	0	0
A4-C2.8	Narrowing section	P7	Upper transitional plug flow to lower transitional plug flow	0	0	0	0
	Narrow section	P3	Lower transitional plug flow to turbulence-enhanced transitional flow	0	0	0	0

4.2. Observed Adaptation Length Scales

The length scales needed by clay flows to adapt to non-uniform conditions can be estimated using the data presented in Figures 9 and 10. The length scales are based on the identified clay-flow types (Table 2) and the distance between the measurement points at locations where a change in velocity is experienced, that is, these estimations involve length scales downstream of the start of the widening section for the decelerating flows and the narrowing section of the accelerating flows, as well as in the wide section for the decelerating flows and in the narrow section for the accelerating flows. The adaptation length scale in the wide (decelerating flow) or narrow section (accelerating flow) is determined by the distance required to develop (nearly) uniform conditions. The adaptation length and time scales are made dimensionless using the standing water depth and the depth-averaged velocity at P2 as characteristic length and time scales (Equations 12 and 13).

For decelerating flows, the adaptation length scales are determined at the widening section and in the wide section as the flow adapts to the change in velocity. As the flow decelerated at the start of the widening section (P3), flow D3-C0.9 changed from turbulent flow to turbulence-enhanced transitional flow, without a significant adaptation length at this position (Figure 9a; Table 3). Throughout the wide section (P7 to P9), the flow adjusted from turbulence-enhanced transitional flow to lower transitional plug flow. Towards the end of the wide section, at P9, $\Delta\mathrm{RMS}(u')_0$ remained non-uniform, suggesting that the length of the flume was insufficient to establish uniform conditions after the widening section (Figure 9a). Hence, the minimum adaptation length needed to change from turbulence-enhanced flow to lower transitional plug flow was 1.4 m, the full distance between P7 and P9 (Figure 2b). At the depth-averaged velocity of 0.28 m/s in the wide section (Table 1), this adaptation length corresponds to a minimum adaptation time of 5.0 s.

Flow D5-C2.7 started to change from a relatively weak to a stronger turbulence-enhanced transitional flow at position P4, that is, 0.7 m into the widening section (Figure 5f), whereas $\Delta\overline{\mathrm{RMS}(u')_0}$ started to increase at P3 in flow D2-C0.0, that is, at the start of the widening section (Figure 4d). The maximum adaptation length this high-concentration clay flow needed after starting to experiencing flow widening was therefore 0.7 m (distance between P3 and P4, Figure 2b). This is equivalent to an adaptation time of 1.4 s at a mean depth-averaged flow velocity of 0.52 m/s between P3 and P4 (Table 1). Flow D5-C2.7 changed from turbulence-enhanced transitional flow via lower transitional plug flow to upper transitional plug flow in the wide section (P7 to P9), without apparently reaching uniform flow conditions (Figure 9b). This is equivalent to a minimum adaptation time of 5.2 s at a depth averaged flow velocity of 0.27 m/s (Table 1) through the 1.4-m long wide section (Figure 2b).

For accelerating flows, the adaptation length scales are determined at the start of the narrowing section and in the narrow section as the flow adapts to the change in velocity. Flow A2-C1.4 changed from lower-transitional plug flow at P6 to turbulence-enhanced transitional flow at P5 in the narrowing section. The distance between P6 and P5 is 0.6 m and with a depth-averaged velocity of 0.26 m/s, this results in an adaptation time of 2.3 s. At the start of the narrow section, P3, flow A2-C1.4 established uniform turbulence-enhanced transitional flow (Figure 10a)

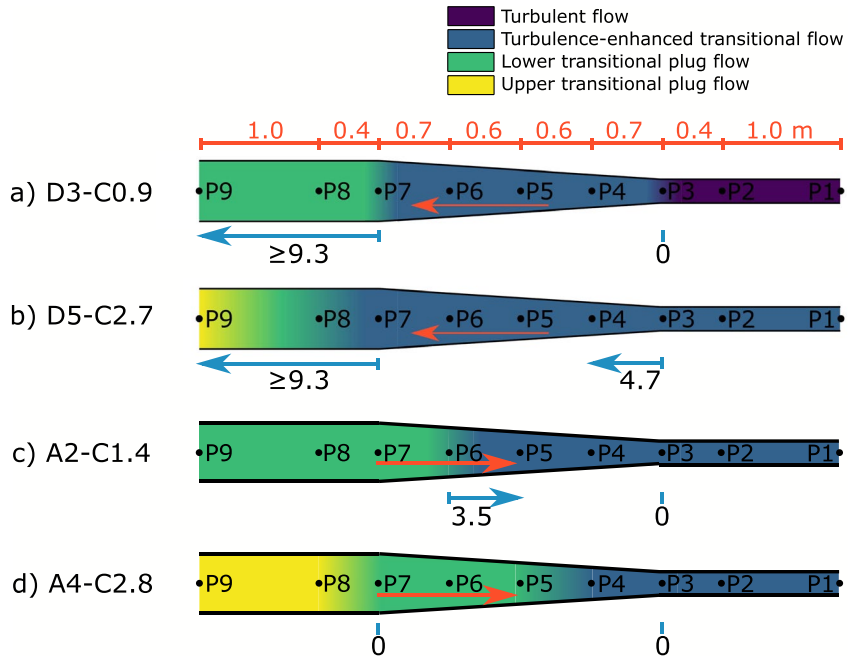

Figure 11. Identified clay flow types and observed dimensionless adaptation length scale, *L*.

and show no adaptation in the narrow section itself. Hence, within the spatial resolution of the experiments, the adaptation length in the narrow section was at or close to zero.

Flow A4-C2.8 started to change from upper transitional plug flow to lower transitional plug flow at the start of the narrowing section at P7 and showed no signs of additional adaptation in the narrowing section (Figure 10b) Hence, the change in clay flow type also lacked a significant delay at this location. At the start of the narrow section, P3, flow A4-C2.8 changed from lower transitional plug flow to turbulence-enhanced transitional flow. Flow A4-C2.8 established uniform turbulence-enhanced transitional flow at the start without additional adaptation in the narrow section. Hence, the change in clay flow type also lacked a significant delay at this location.

4.3. Implications of Adaptation Length Scales

Figure 11 shows an overview of the clay flow types in the experimental runs and the dimensionless adaptation length scales. The adaptation length and time scales show that the decelerating flows generally needed longer to adapt to the imposed non-uniform conditions than the accelerating flows (Figure 11, Table 3). The largest adaptation lengths and times were at the end of the widening section in the decelerating flows, where the flows changed from turbulence-enhanced transitional flow to more cohesive lower and upper transitional plug flows. In contrast, the accelerating flows changed from the more cohesive lower transitional plug flow to turbulence-enhanced flow already in the narrowing section. These differences in adaptation length between the decelerating and accelerating flows can be explained by the fact that establishing cohesive bonds between clay particles, as in the decelerating flows, requires more time than breaking up these bonds, as in the accelerating flows.

Stronger turbulence attenuated flow types are identified in the clay flows with higher clay concentrations. It appears to take longer to establish a pervasive network of clay bonds, as in the change from turbulence-enhanced transitional flows to lower and upper transitional plug flow at the end of the widening section in the decelerating flows, than to establish a turbulence-enhanced transitional flow from a turbulent flow by reducing the flow velocity in low-concentration clay flows (e.g., Figure 9a).

The research focus here is on adaptation of flow dynamics of non-uniform clay-laden flows, but the length and time scales of flow adaptation can also be reflected in the depositional product (Dorrell & Hogg, 2012). Here, non-uniformity on spatial deceleration and acceleration in clay-laden open-channel demonstrates that these adaptation scales in mud-rich flows fundamentally differ between decelerating and accelerating regimes, due to the

time required to form or break cohesive bonds between particles. These results are based on streamwise velocity measurements due to the limitations of Ultrasonic Velocity Profilers, which are designed to work along a single beam. Further developments in technology are needed to fully resolve the turbulent motion of highly concentrated flows.

Additional research in the sedimentological record is required to determine how deposits of non-uniform clay suspension flows can be recognized in fluvial, estuarine and submarine systems. For example, after a sediment supply increase in a river following wild-fire related erosion (Nyman et al., 2019; Renau et al., 2007; Sankey et al., 2017), flow deceleration can occur following for example, a reduction in bed slope or widening of the river channel. The flow deceleration reduces the turbulent forces in the flow and allows the establishment of cohesive bonds between clay particles. The adaptation to stronger turbulence attenuated clay flow types requires time due to the formation of clay bonds and consequently, the deposits associated with the clay flow type form over the adaptation length scale downstream of the location of flow deceleration. In an industrial setting, such as downstream of dam flushing or venting events, flow acceleration can occur (Antoine et al., 2020), increasing the turbulent forces in the flow, which has the potential to break up bonds between clay particles. This study shows that the adaptation of the clay flow type to a stronger turbulent flow occurs more rapidly and consequently the associated deposits with clay flow type occur near the location of acceleration. Additionally, the different adaptation length and time scales are of particular relevance in interpreting the shape of submarine deposits, such as unconfined submarine lobes (Spychala et al., 2017) and hybrid event beds deposited around diapirs (Davis et al., 2009; Patacci et al., 2014). It is anticipated that the depositional record of decelerating flows reflects the time scales required to form interparticle bonds, delaying the depositional response to the associated changes in flow conditions. For accelerating flows, it is anticipated that changes in deposit properties associated with bond breakage occur more rapidly, such that they are more closely associated with the areas where acceleration occurs.

5. Conclusions

This research investigated the influence of suspended cohesive clay on changing flow dynamics under non-uniform flow conditions using decelerating and accelerating open-channel flows in a recirculating flume. These flows may evolve through different clay flow types with different associated degrees of turbulence enhancement and attenuation depending on the clay concentration and whether the flows decelerate or accelerate. Decelerating flows have a longer adaptation time than accelerating flows as establishing cohesive bonds between clay particles requires more time than breaking the clay bonds. This hysteresis is more pronounced for higher-concentration flows that change from the turbulence-enhanced transitional flow type to the lower and upper transitional plug flow types than for lower-concentration decelerating flows that change from the turbulent flow type to the turbulence-enhanced transitional flow type. Differences in adaptation time likely influence the distribution and character of deposit in sedimentary environments. The associated deposits with clay flow type of decelerating flows are likely spread over a larger distance than that of accelerating flow due to the elongated adaptation time of decelerating flows.

Data Availability Statement

The data collected during the physical experiments in preparation for this research is available at https://doi.org/10.5281/zenodo.6642324 (Cite as: de Vet et al., 2022).

Acknowledgments
This work was carried out as part of a PhD studentship, part funded through the Turbidites Research Group, University of Leeds and part funded through the University of Hull. Bangor University is thanked for the loan of Ultrasonic Velocity Profilers for the duration of the experiments. RMD is grateful for funding from NERC NE/S014535/1. Participation of RF in this study has been possible thanks to The Leverhulme Trust, Leverhulme Early Career Researcher Fellowship (grant ECF-2020-679) and the European Research Council under the European Union's Horizon 2020 research and innovation program (Grant 725955).

References

Ackers, J., Butler, D., Leggett, D., & May, R. (2001). *Designing sewers to control sediment problems* (pp. 818–823). Urban Drainage Modeling. https://doi.org/10.1061/40583(275)77

Antoine, G., Camenen, B., Jodeau, M., Nemery, J., & Esteves, M. (2020). Downstream erosion and deposition dynamics of fine suspended sediments due to dam flushing. *Journal of Hydrology*, *585*, 124763. https://doi.org/10.1016/j.jhydrol.2020.124763

Baas, J. H., & Best, J. L. (2002). Turbulence modulation in clay-rich sediment-laden flows and some implications for sediment deposition. *Journal of Sedimentary Research*, *72*(3), 336–340. https://doi.org/10.1306/120601720336

Baas, J. H., Best, J. L., Peakall, J., & Wang, M. (2009). A phase diagram for turbulent, transitional, and laminar clay suspension flows. *Journal of Sedimentary Research*, *79*(4), 162–183. https://doi.org/10.2110/jsr.2009.025

Bagnold, R. A. (1954). Experiments on a gravity-free dispersion of large, solid spheres in a Newtonian fluid under shear. *Proceedings of the Royal Society of London, Series A: Mathematical and Physical Sciences*, *225*(1160), 49–63. https://doi.org/10.1098/rspa.1954.0186

Barbero, R., Abatzoglou, J. T., Larkin, N. K., Kolden, C. A., & Stocks, B. (2015). Climate change presents increased potential for very large fires in the contiguous United States. *International Journal of Wildland Fire*, *24*(7), 892–899. https://doi.org/10.1071/WF15083

Best, J., Bennet, S., Bridge, J., & Leeder, M. R. (1997). Turbulence modulation and particle velocities over flat sand beds at low transport rates. *Journal of Hydraulic Engineering*, *123*(12), 1118–1129. https://doi.org/10.1061/(ASCE)0733-9429(1997)123:12(1118)

Best, J. L., Kirkbridge, A. D., & Peakall, J. (2001). Mean flow and turbulence structure of sediment-laden gravity currents: New insights using ultrasonic Doppler velocity profiling. In W. D. McCaffrey, B. C. Kneller, & J. Peakall (Eds.), *Particulate gravity currents* (Vol. 31, pp. 159–172). International Association of Sedimentologists, Special Publication. https://doi.org/10.1002/9781444304275.ch12

Best, J. L., & Leeder, M. R. (1993). Drag reduction in turbulent muddy seawater flows and some sedimentary consequences. *Sedimentology*, *40*(6), 1129–1137. https://doi.org/10.1111/j.1365-3091.1993.tb01383.x

Cardoso, A. H., Graf, W. H., & Gust, G. (1991). Steady gradually accelerating flow in a smooth open channel. *Journal of Hydraulic Research*, *29*(4), 525–543. https://doi.org/10.1080/00221689109498972

Davis, C., Haughton, P., McCaffrey, W., Scott, E., Hogg, N., & Kitching, D. (2009). Character and distribution of hybrid sediment gravity flow deposits from the outer Forties Fan, Paleocene Central North Sea, UKCS. *Marine and Petroleum Geology*, *26*(10), 1919–1939. https://doi.org/10.1016/j.marpetgeo.2009.02.015

Dorrell, R. M., Amy, L. A., Peakall, J., & McCaffrey, W. D. (2018). Particle size distribution controls the threshold between net sediment erosion and deposition in suspended load dominated flows. *Geophysical Research Letters*, *45*(3), 1443–1452. https://doi.org/10.1002/2017GL076489

Dorrell, R. M., & Hogg, A. J. (2012). Length and time scales of response of sediment suspension to changing flow conditions. *Journal of Hydraulic Engineering*, *138*(5), 430–439. https://doi.org/10.1061/(ASCE)HY.1943-7900.0000532

Geertsema, M., Clague, J. J., Schwab, J. W., & Evans, S. G. (2006). An overview of recent large catastrophic landslides in northern British Colombia, Canada. *Engineering Geology*, *83*(1–3), 120–143. https://doi.org/10.1016/j.enggeo.2005.06.028

Kironoto, B. A., & Graf, W. H. (1995). Turbulence characteristics in rough non-uniform open-channel flow. *Proceedings of the Institute of Civil Engineers Water Maritime and Energy*, *112*(4), 336–348. https://doi.org/10.1680/iwtme.1995.28114

Li, M. Z., & Gust, G. (2000). Boundary layer dynamics and drag reduction in flows of high cohesive sediment suspensions. *Sedimentology*, *47*(1), 71–86. https://doi.org/10.1046/j.1365-3091.2000.00277.x

Mehta, A. J., McAnally, W. H., Jr., Hayter, E. J., Teeter, A. M., Schoellhamer, D., Heltzel, S. B., & Carey, W. P. (1989). Cohesive sediment transport. II: Application. *Journal of Hydraulic Engineering*, *115*(8), 1094–1112. https://doi.org/10.1061/(ASCE)0733-9429(1989)115:8(1094)

Moody, J. A., Shakesby, R. A., Robichaud, P. R., Cannon, S. H., & Martin, D. A. (2013). Current research issues related to post-wildfire runoff and erosion processes. *Earth-Science Reviews*, *122*, 10–37. https://doi.org/10.1016/j.earscirev.2013.03.004

Nezu, I., & Nakagawa, H. (1993). *Turbulence in open-channel flows*. Delft Hydraulics, International Association for Hydraulic Research.

Nyman, P., Box, W. A. C., Stout, J. C., Sheridan, G. J., Keestra, S. D., Lane, P. N. J., & Langhans, C. (2019). Debris-flow-dominated sediment transport through a channel network after wildfire. *Earth Surface Processes and Landforms*, *45*(5), 115–1167. https://doi.org/10.1002/esp.4785

Partheniades, E. (1965). Erosion and deposition of cohesive soils. *Journal of the Hydraulics Division*, *91*(1), 105–139. https://doi.org/10.1061/JYCEAJ.0001165

Partheniades, E. (2009). *Cohesive sediment in open channels*. Butterworth-Heinemann.

Patacci, M., Haughton, P. D. W., & McCaffrey, W. D. (2014). Rheological complexity in sediment gravity flows to decelerate against a confiing slope, Braux, SE France. *Journal of Sedimentary Research*, *84*(4), 270–277. https://doi.org/10.2110/jsr.2014.26

Qingyang, S. (2009). Velocity distribution and wake-law in gradually decelerating flows. *Journal of Hydraulic Research*, *47*(2), 177–184. https://doi.org/10.3826/jhr.2009.3254

Reneau, S. L., Katzman, D., Kuyumjian, G. A., Lavine, A., & Malmon, D. V. (2007). Sediment delivery after a wildfire. *Geology*, *35*(2), 151–154. https://doi.org/10.1130/G23288A.1

Sankey, J. B., Kreitler, J., Hawbaker, T. J., McVay, J. L., Miller, M. E., Mueller, E. R., et al. (2017). Climate, wildfire, and erosion ensemble foretells more sediment in western USA watersheds. *Geophysical Research Letters*, *44*(17), 8884–8892. https://doi.org/10.1002/2017GL073979

Smith, H. G., Sheridan, G. J., Lane, P. N. J., Nyman, P., & Haydon, S. (2011). Wildfire effects on water quality in forest catchments: A review with implications for water supply. *Journal of Hydrology*, *396*(1–2), 170–192. https://doi.org/10.1016/j.jhydrol.2010.10.043

Spychala, Y. T., Hodgson, D. M., Prelat, A., Kane, I. A., Flint, S. S., & Mountney, N. P. (2017). Frontal and lateral submarine lobe fringes: Comparing sedimentary facies, architecture and flow processes. *Journal of Sedimentary Research*, *87*(1), 75–96. https://doi.org/10.2110/jsr.2017.2

Swanson, F. J. (1981). Fire and geomorphic processes. In H. A. Mooney, T. M. Christensen, J.E. Lotan, & W. A. Reiners (Eds.), *Fire regimes and ecosystem properties* (pp. 401–444). U.S. Department of Agriculture Forest Service General Technical Report WO-26.

Takeda, Y. (1991). Development of an ultrasound velocity profile monitor. *Nuclear Engineering and Design*, *126*(2), 277–284. https://doi.org/10.1016/0029-5493(91)90117-Z

Talling, P. J., Masson, D. G., Sumner, E. J., & Malgesini, G. (2012). Subaquous sediment density flows: Depositional processes and deposit types. *Sedimentology*, *59*(7), 1937–2003. https://doi.org/10.1111/j.1365-3091.2012.01353.x

Van Olphen, H. (1977). *An introduction to clay colloid chemistry* (2nd ed.). John Wiley & Sons.

Wan, Z. (1982). *Bed material movement in hyperconcentrated flows, Serie paper 31*. Institute of Hydrodynamics and Hydraulic Engineering. Technical University of Denmark.

Wang, Z., & Larsen, P. (1994). Turbulence structure of flows of water and clay suspensions with bedload. *Journal of Hydraulic Engineering*, *120*(5), 577–600. https://doi.org/10.1061/(ASCE)0733-9429(1994120:5(577)

Whitehouse, R. J. S., Soulsby, R. L., Roberts, W., & Mitchener, H. J. (2000). *Dynamics of estuarine muds*. Technical Report. Thomas Telford.

Winterwerp, J. C., & van Kesteren, W. G. M. (2004). *Introduction to the physics of cohesive sediment in the marine environment* (Vol. 56). Elsevier. Developments in Sedimentology.